Strong single-ion anisotropy and anisotropic interactions of magnetic adatoms induced by topological surface states

Z. L. Li,[1] J. H. Yang,[1] G. H. Chen,[1] M.-H. Whangbo,[2] H. J. Xiang,[1,*] and X. G. Gong[1,†]

[1]*Key Laboratory of Computational Physical Sciences (Ministry of Education), State Key Laboratory of Surface Physics, and Department of Physics, Fudan University, Shanghai 200433, People's Republic of China*

[2]*Department of Chemistry, North Carolina State University, Raleigh, North Carolina 27695-8204, USA*

The nature of the magnetism brought about by Fe adatoms on the surface of the topological insulator Bi_2Se_3 was examined in terms of density functional calculations. The Fe adatoms exhibit strong easy-axis magnetic anisotropy in the dilute adsorption limit due to the topological surface states (TSS). The spin-exchange J between the Fe adatoms follows a Ruderman-Kittel-Kasuya-Yosida behavior with substantial anisotropy, and the Dzyaloshinskii-Moriya interaction between them is quite strong with $|D/J| \approx 0.3$ under the mediation by the TSS and can be further raised to ~ 0.6 by an external electric field. The apparent single-ion anisotropy of a Fe adatom is indispensable in determining the spin orientation.

PACS number(s): 73.20.−r

I. INTRODUCTION

In a topological insulator (TI), the bulk state has a band gap, but the topological surface state (TSS) is gapless due to the protection by the time reversal symmetry (TRS). In three-dimensional (3D) TI's, Bi_2Se_3, Bi_2Te_3, and Sb_2Te_3,[1] the bulk band gap is nontrivial, and the TSS is robust with a single Dirac cone at Γ point[2–4] that originates from spin-orbit coupling (SOC).[5] The TRS of a TI can be broken by introducing magnetic atoms on its surface,[6–12] leading to a band-gap opening at the Dirac point so that TIs with their surface doped with magnetic atoms can provide useful spintronics applications.[6,11] The interactions between magnetic adatoms on a TI surface are known to follow a Ruderman-Kittel-Kasuya-Yosida (RKKY) behavior.[8,9,11] In describing these interactions using a model $\boldsymbol{k} \cdot \boldsymbol{p}$ Hamiltonian, both the anisotropic (Heisenberg-Ising) spin exchange and the antisymmetric Dzyaloshinskii-Moriya (DM) exchange are taken into consideration.[11] As for the preferred spin orientation, described by the single-ion anisotropy (SIA), of magnetic adatoms, which opens a gap at the Dirac point when their spins are parallel to the c axis,[3] there exists controversy.[3,7] In accounting for the magnetism mediated by the TSS, therefore, it is necessary to investigate it on the basis of first-principles methods without neglecting the SIA.

In this paper, we investigate the nature of the magnetism arising from magnetic adatoms on a TI surface by performing first-principles calculations based on density functional theory (DFT) for Bi_2Se_3 with magnetic Fe atoms adsorbed on its (111) surface and by analyzing results of the calculations in terms of the energy-mapping method.[13] We show that in the dilute adsorption limit, a Fe adatom exhibits a strong easy-axis SIA because of the spin-polarized Bi and Se atoms surrounding it, the spin-exchange J between the magnetic adatoms is strongly anisotropic and follows a RKKY-like behavior, and the DM interaction between them is strong with $|D/J| \approx 0.3$ because of the mediation by the TSS and can be enhanced further by external electric field, indicating potential applications of TI's with magnetic adatoms on their surface to spintronics.

This work is organized as follows. We describe our computational methods and the structure models in Sec. II, and analyze the electronic structures of pristine Bi_2Se_3 and Fe-adsorbed Bi_2Se_3 in Sec. III. Sec. IV shows that Fe exhibits an apparently large SIA when adsorbed on the surface of Bi_2Se_3 due to the Fe-induced spin polarization and the SOC of the TSS. The TSS-mediated interactions between the two Fe atoms adsorbed on Bi_2Se_3 are discussed in Sec. V, and how these interactions and the apparent SIA compete and determine the spin orientation of the Fe-adatom pair in Sec. VI. In Sec. VII we show that the TSS-mediated interactions between the Fe adatoms and the magnetization of them are delicately controllable by an external electric field. Results validating our computational models are presented in Sec. VIII, and the results of our study are summarized in Sec. IX.

II. COMPUTATIONAL METHODS AND GEOMETRICAL STRUCTURES

Our density functional calculations were performed using the Vienna *ab initio* simulation package[14] with the projector-augmented-wave method,[15,16] the generalized-gradient approximation by Perdew, Burke, and Ernzerhof[17] for exchange-correlation functional, and a plane-wave cutoff energy of 340 eV. Experimentally, Bi_2Se_3 with a few quintuple layers (QL's) or even only one QL were prepared to study the TSS.[2,18] In this paper, we simulate the (111) surface of Bi_2Se_3 by using a slab of one quintuple layer (1QL-slab) of Bi_2Se_3 with the vacuum layer more than 10 Å. The structure of 1QL-slab with Fe atoms adsorbed on one surface was fully relaxed using one k point (i.e., Γ). With the resulting optimized structure, $4 \times 4 \times 1$ supercell calculations were carried out using a set of $3 \times 3 \times 1$ k points for one Fe adsorption per supercell as well as for cases of two Fe adatoms per supercell when the distance R between them is short. However, $8 \times 4 \times 1$ supercell calculations were performed using a set of $2 \times 3 \times 1$ k points for cases of two Fe adatoms per supercell if their distance R is large (see Sec. V). The use of the large supercells is necessary to simulate the dilute adsorption limit. All calculations were performed, including SOC on all atoms unless otherwise stated. In our calculations the effect of an external electric field along the c direction was included by using the planar
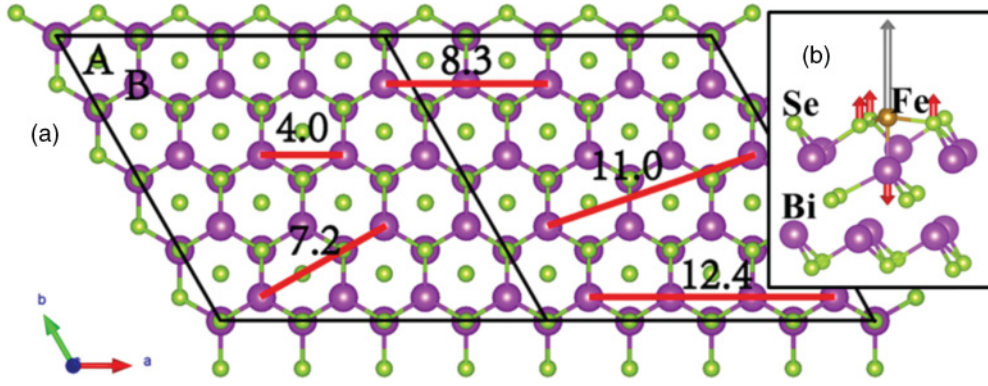
FIG. 1. (Color online) (a) A top view of the pristine (111) surface of Bi_2Se_3. A and B represent the two possible adsorption sites for a magnetic Fe atom. The positions for various pairs of Fe atoms at the B sites are indicated by red segments with their optimized distances in units of angstroms. (b) A side view of a 1QL-slab with a single isolated Fe adatom showing the distorted local structure around the Fe atom. The spin of Fe (gray arrow) induces spin polarization to Bi^* and Se^*, leading to small moments (red arrows/dark gray) on them. The spin-polarized spin moments of Bi^* and Se^* are antiparallel and parallel to that of Fe, respectively.

dipole layer method.[19] We also simulated the Fe-adsorbed (111) surface of Bi_2Se_3 by using a slab of two QL's (2QL-slab) and that of four QL's (4QL-slab), to find that the use of the 1QL-slab model for the (111) surface of Bi_2Se_3 is sufficient for discussing the problems under consideration (see Sec. VIII).

The top views of the 4×4 and 8×4 supercells of the pristine (111) surface of Bi_2Se_3 are presented in Fig. 1(a). Each QL has the layer sequence Se-Bi-Se-Bi-Se. We considered two possible adsorption sites on the (111) surface of Bi_2Se_3 [A and B in Fig. 1(a)]. The A sites are the hollow sites of the nearest-neighbor Se_3 triangles on the surface Se layer, while the B sites are the on-top sites of the Bi atoms. Our calculations show that each Fe prefers the B-site adsorption to the A-site adsorption by 75.8 meV. Thus, hereafter, we will assume the B-site adsorption of Fe atoms unless otherwise stated. We denote the Bi and Se atoms adjacent to the Fe adatom at the B site as Bi^* and Se^*, respectively. The Fe atom lies slightly (0.268 Å) above the center of the Se^*_3 triangle, and the Bi^* atom goes down by 0.753 Å from the position of the pristine 1QL-slab [Fig. 1(b)]. Without loss of generality, we take the local z axis along the c axis and set the positive x axis for a Fe atom pair along the dimer (i.e., $\mathbf{R} = \mathbf{r}_2 - \mathbf{r}_1$).

III. ELECTRONIC STRUCTURE

The band structure calculated for the pristine 1QL-slab [Fig. 2(a)] shows a band gap of 0.5 eV in agreement with the experiment.[18] The lower Dirac cone disappears for the 1QL-slab,[2,18] so only the upper Dirac cone is present in Fig. 2(a). The major components of this band are the $6p_z$ orbitals of the Bi atoms and the $4p_x/4p_y$ orbitals of the surface Se atoms. This surface band consists of the spin-up and spin-down bands that are degenerate. The band structure of the 1QL-slab with a single Fe adsorbed in a $4 \times 4 \times 1$ supercell [Fig. 2(b)] shows a splitting of the spin-up and spin-down Dirac bands, which is due largely to their strong interactions with the spin-polarized Fe $3d_{z^2}$ states. The Fe $3d_{z^2}$ interacts with the Bi^* $6p_z$ and the Fe $3d_{xy}$ and $3d_{x^2-y^2}$ with the Se^* $4p_x$ and $4p_y$. Consequently, the spin-polarized electrons of the Fe adatom interact strongly with the conducting electrons of the TSS. The

calculated moment of the Fe adatom (~ 2.9 μ_B) suggests the presence of approximately three unpaired electrons at the Fe site. The projected density of states (PDOS) calculated for the Fe 3d states [Fig. 2(c)] suggests an approximate crystal-field split pattern of the Fe 3d states depicted in Fig. 2(d). The approximate electron configuration of Fe is a high spin in between (d^6) and (d^7).

IV. APPARENT SINGLE-ION ANISOTROPY

In opening a gap at the Dirac point by magnetic adatoms, it is necessary that the adatoms have the $//c$ spin orientation.[3] To determine the preferred spin orientation due to the SOC effect, we calculate the SIA energy, $A = E_{//c} - E_{\perp c}$, using one Fe adatom per 4×4 supercell, where $E_{//c}$ and $E_{\perp c}$ are the energies with adatom spin orientation parallel and perpendicular to the c axis, respectively. Our calculations show that $A = -5.80$ meV per Fe adatom for the B-site adsorption ($A = -5.16$ meV per Fe adatom for the A-site adsorption) when SOC effects are included on both the adatom Fe and the host Bi_2Se_3, showing that the Fe spin strongly prefers to align along the c direction. Therefore, our finding is entirely consistent with the experimental observation of a massive Dirac fermion state in Bi_2Se_3 by chemical vapor deposition of Fe atoms on its (111) surface.[3] The above calculation of the SIA energy is for dilute adsorption coverage (6.25% for one Fe adatom per 4×4 supercell). Thus, the effect of the spin exchange on the SIA energy would be negligible (see Sec. V).

We now examine why a Fe adatom on Bi_2Se_3 (111) surface exhibits apparently a large SIA energy by considering the B-site adsorption. Table I presents the SIA energies calculated by including SOC effects on different atoms, which show that the apparent SIA of a Fe adatom arises largely from the Bi^* and Se^* atoms surrounding it. Because the spin-orbit interaction is a local interaction,[20] our calculations indicate that the magnetic atom Fe induces spin polarization largely on the Bi^* and Se^* atoms, which gives rise to small spin moments (~ 0.055 μ_B) collinear with that of Fe on them [Fig. 1(b)], and the SOC associated with these small spin moments of Bi^* and Se^* leads to the apparent SIA of the Fe adatom. To demonstrate that
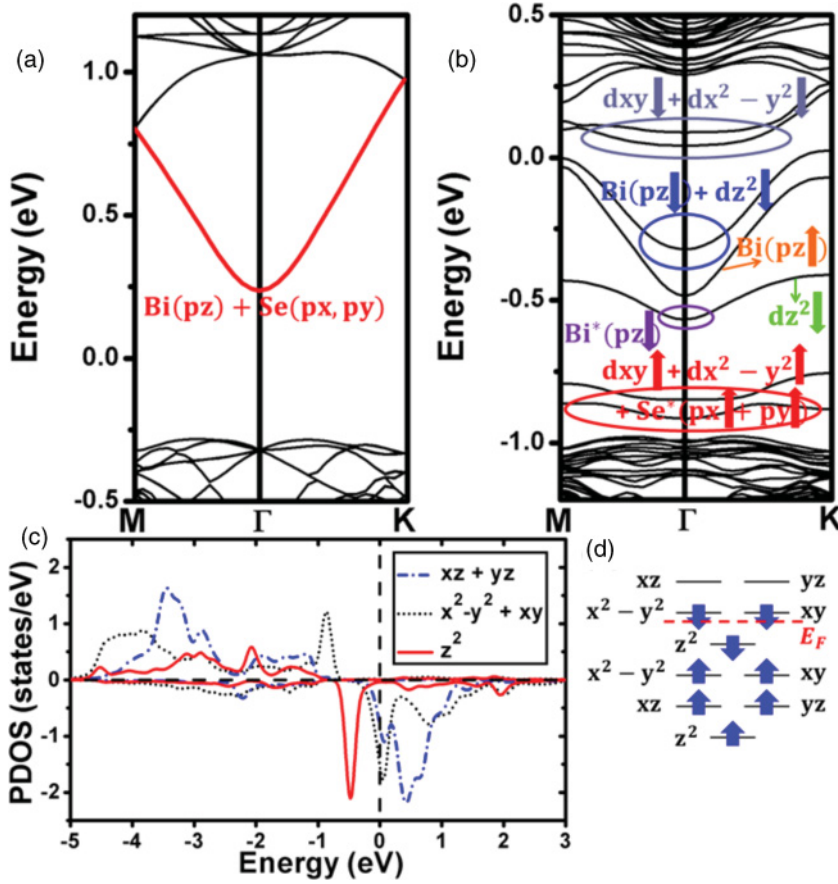
FIG. 2. (Color online) (a) The band structure calculated for the pristine 1QL-slab of Bi_2Se_3. The main surface components are marked in red/dark gray. (b)–(d) show the electronic structure of the 1QL-slab of Bi_2Se_3 with a single Fe atom adsorbed on the surface at the B site. (b) The band structure showing that the Fe 3d states interact strongly with the 6p states of the Bi^* atom and the 4p states of the Se^* atoms. (c) The PDOS plots for the 3d states of the adsorbed Fe atom. (d) An approximate crystal-field split pattern for the 3d states of the adsorbed Fe atom and their electron occupation.

the polarization of the TSS, induced by Fe, leads to a strong apparent SIA, we consider the SOC effect on the p-states of Bi^* as a representative example.

The PDOS plots calculated for the p-states of Bi^* (Fig. 3) around the Fermi level reveal that the three p-states $|p_z, \uparrow\rangle$, $|p_x, \downarrow\rangle$, and $|p_y, \downarrow\rangle$ of Bi^* are nearly degenerate in the absence of SOC on Bi_2Se_3 but become split in the presence of SOC on Bi_2Se_3. We now examine this observation by considering how the three states become split under the action of SOC on Bi^* using the spin-orbit Hamiltonian $H_{SO} = \lambda L \cdot S$, where λ is the SOC constant ($\lambda > 0$ for the case of one electron occupying the three p-states; see details in Appendix A).

After SOC is turned on, the three degenerate states split with two different split patterns for the //c spin orientation ($\theta = 0$, where θ is the angle between the spin and the local z axis, i.e., the c axis) and the $\perp$c spin orientation ($\theta = \frac{\pi}{2}$). The split patterns of these two situations are shown in Fig. 4 (see details in Appendix A). In our case, if there is one electron sharing these three states, under the effects of SOC, the spin of this

electron prefers //c orientation with more energy gain. Note that the above discussion is valid for any fractional electron occupancy (less than two) of the three levels, although we discussed as if there exists one whole electron to occupy them. The effect of SOC on the p-states of Se^* can be discussed in a similar manner (not shown). Because the polarized spin moments of Bi^* and Se^* prefer //c orientation under SOC, and the spins of Bi^* and Se^* are collinear with that of Fe, thus the Fe spin has a //c orientation preference. In other words, the contributions of the Fe, Bi^*, and Se^* should be taken together as a whole in considering the SIA of a magnetic adatom Fe.

Our result from first-principles calculations is consistent with the above conclusion that the Fe spin favors the //c orientation. We also find a slight in-plane anisotropy of the $E_{\perp c}$ term, which could be depicted as an A vs ϕ curve, as presented in Fig. 5. This in-plane anisotropy is substantial for the B-site adsorption of Fe but negligible for the A-site adsorption. Nevertheless, the variation of this in-plane anisotropy (from -5.08 to -6.51 meV) for the B-site adsorption is small compared with the SIA, and we neglect it by taking the average of the $E_{\perp c}$ values along the x and y axes throughout this paper.

V. INTERACTION BETWEEN ADATOMS

To describe how two magnetic adatoms interact on the surface of a TI, we use the Hamiltonian[13,20,21]

$$H = \left(J_{zz}S_1^z S_2^z + J_{xx}S_1^x S_2^x + J_{yy}S_1^y S_2^y\right) + \mathbf{D} \cdot (\mathbf{S}_1 \times \mathbf{S}_2) + A\left[\left(S_1^z\right)^2 + \left(S_2^z\right)^2\right], \quad (1)$$

TABLE I. The calculated SIA energy of a single isolated Fe ion at B site on the surface of Bi_2Se_3. We include SOC on different atoms: (i) the host Bi_2Se_3 and Fe, (ii) host only, (iii) Fe only, and (iv) Fe, adjacent Bi^*, and Se^*, respectively, to examine the origin of the strong SIA.

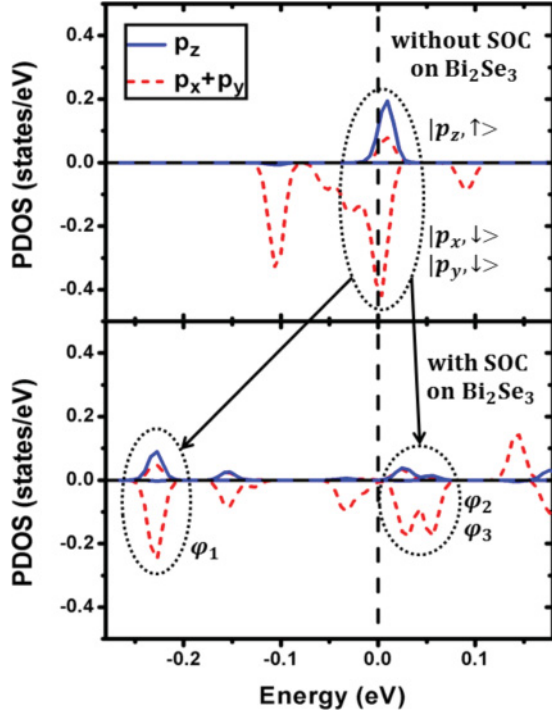| SOC	Host and Fe	Host only	Fe only	Fe, Bi^*, and Se^*
A (meV)	-5.8	-4.9	-1.7	-4.9

FIG. 3. (Color online) The PDOS plots calculated for the p-states of Bi* near the Fermi level before and after including SOC. In the absence of SOC, the $|p_z, \uparrow\rangle$, $|p_x, \downarrow\rangle$, and $|p_y, \downarrow\rangle$ states located around the Fermi level are practically degenerate. These states are split in energy when SOC is included.

where the first term describes the Heisenberg-Ising spin exchange between the adatoms, the second term describes the DM interaction between them, and the last term is the SIA of the two adatoms, which should be included in model Hamiltonian analysis because it is very large.[20] To determine the parameters J_{ii} (i = x, y, z), **D** and A, we carry out

energy-mapping analysis[13] on the basis of density functional calculations by treating the spin as unit vectors, i.e., $|\mathbf{S}_i| = 1$ (i = 1, 2). (See calculation methods of this section in Appendix B.) As shown in Fig. 1(a), we consider five different pairs of Fe adatoms at the B-sites and evaluate their J_{ii} (i = x, y, z) values. For a pair of Fe adatoms occupying nearest-neighbor B sites, the relaxed distance R is 4.009 Å (hereafter R ≈ 4.0 Å), slightly shorter than the lattice constant 4.138 Å. In calculating the J_{ii} values, we use the 4 × 4 × 1 supercell for the adatom pairs with R ≈ 4.0 and 7.2 Å, and the 8 × 4 × 1 supercell for those with R ≈ 8.3, 11.0 and 12.4 Å to avoid the direct interaction between adjacent pairs.

For the pair with R ≈ 4.0 Å, the spin exchanges are antiferromagnetic (AFM) and anisotropic. From Table II, if the SOC on Fe is switched off and only kept on the host Bi_2Se_3, these spin exchanges hardly change. However, on switching off the SOC on the host Bi_2Se_3 and keeping that of Fe, the spin exchanges and their anisotropy become strongly reduced. Thus, the conducting electrons of the TSS enhance the spin exchanges and also introduce anisotropy to the exchanges between the Fe adatoms. For the Fe adatom pair with R ≈ 7.2 Å, the spin exchanges are ferromagnetic (FM) and anisotropic. As summarized in Fig. 6 for the J_{zz} values, as an example, the sign of the spin exchange oscillates as R increases, following a RKKY behavior. This is in agreement with the conclusion from the model Hamiltonian studies.[8,9,11] The J_{zz} values calculated without SOC on all atoms, also plotted in Fig. 6, show that the spin exchanges between adatoms are still strong even without SOC and follow a RKKY behavior. Namely, under the mediation of the TSS electrons, the spin exchange is a long-range interaction.[3,11]

The DM vector $\mathbf{D} = (D_x, D_y, D_z)$ is also evaluated by performing energy-mapping analysis[13] (Appendix B). Symmetry analysis (Appendix B) of the structures of the Fe adatom dimers shows that $D_x = 0$ for R ≈ 4.0 Å and $D_x = D_z = 0$ for R ≈ 7.2 Å. The calculated DM vectors (see Table II) are
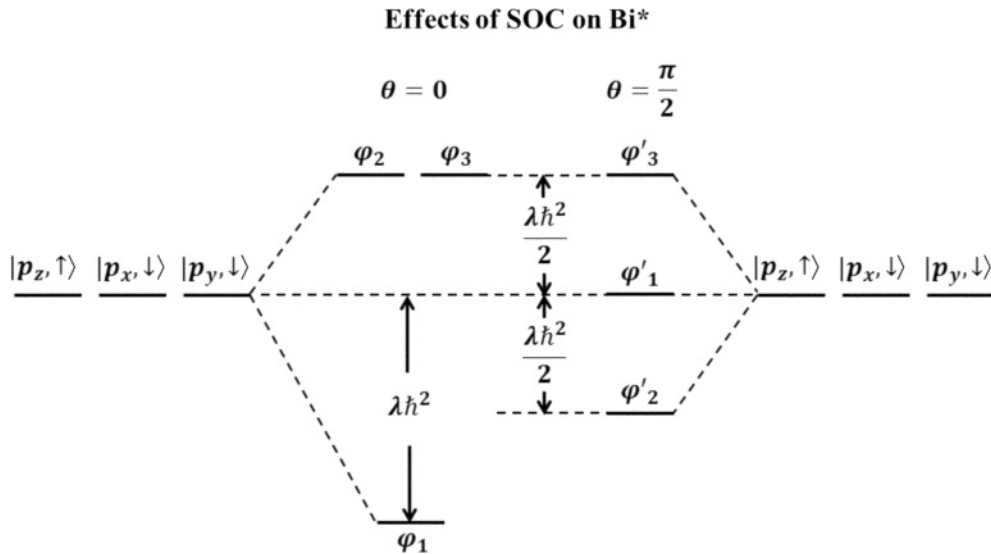

FIG. 4. The split patterns of the three p-states of Bi* near the Fermi level (namely, $|p_z, \uparrow\rangle$, $|p_x, \downarrow\rangle$, and $|p_y, \downarrow\rangle$) under the effect of SOC when the spin orientation is along the z axis ($\theta = 0°$) and perpendicular to the z axis ($\theta = \frac{\pi}{2}$). (Note that the local z axis is parallel to the c axis.) With one electron to occupy the resulting three states, the SOC favors the z axis orientation, i.e., //c SIA.
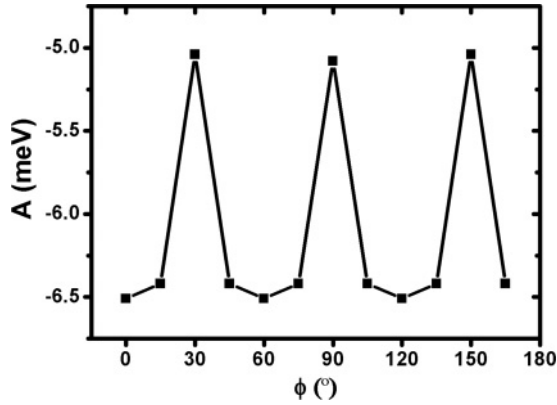
FIG. 5. The SIA A vs ϕ curve calculated for the Fe adatom adsorbed on the B-site of Bi_2Se_3 (111), where the in-plane sweep angle ϕ is defined such that the direction for $\phi = 0°$ is parallel to one Se^*-Se^* edge of the Se^*_3 triangle.
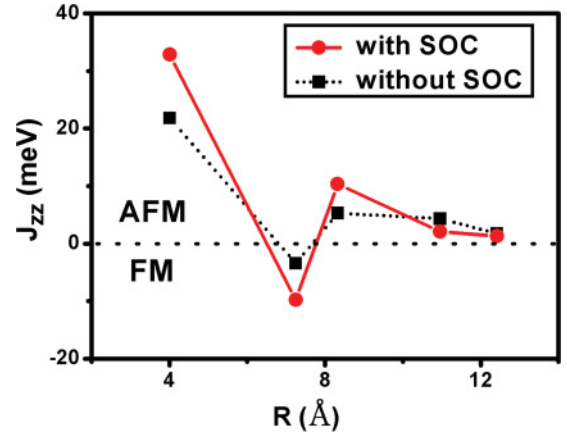

FIG. 6. (Color online) The dependence of the spin-exchange J_{zz} between two Fe atoms adsorbed on the (111) surface on the distance R between them, calculated with and without SOC effects.

consistent with this analysis. The nonzero component of the **D** vector is quite large compared with the spin exchange, i.e., $|D/J_{ave}| \approx 0.3$, where J_{ave} is the average of J_{xx}, J_{yy}, and J_{zz}. To understand the origin of this large DM interaction, we selectively include the SOC on different atoms and switch off that on others by considering the Fe dimer with $R \approx 4.0$ Å as an example, and the results are also listed in Table II. The calculations show the large D_y originates from the TSS because D_y is very large when the SOC of the host Bi_2Se_3 is kept but almost zero when that is switched off. This conclusion is consistent with that of Zhu *et al.*[11] who predicted the along the y axis DM interaction. Also, we found the small D_z basically comes from the SOC of Fe pair itself. Thus, the strong DM interactions are also mediated by the conducting electrons of the TSS.

For the cases of two Fe adatoms on the (111) surface, the SIA A can also be evaluated by energy-mapping analysis (Appendix B), which shows that A depends on their distance R (Table II). Nevertheless, the preference for the $//c$ spin orientation at the B-sites remains unaffected by the interactions between the adatoms mediated by the TSS electrons or by the thickness of the slab used for calculations (see Sec. VIII).

TABLE II. The model parameters of the Hamiltonian from the energy-mapping analysis. The results for the two pairs with different pair distances are shown. For the $R \approx 4.0$ Å case, we also include SOC on different atoms.

Pair distance	$R \approx 4.0$ Å			$R \approx 7.2$ Å
SOC on	Host and Fe	Host only	Fe only	Host and Fe
J_{xx} (meV)	34.9	34.7	18.8	−10.0
J_{yy} (meV)	27.1	26.9	18.8	−15.3
J_{zz} (meV)	32.9	32.9	18.3	−9.8
D_x (meV)	0	—	—	−0.1
D_y (meV)	−10.1	−10.8	−0.7	3.8
D_z (meV)	1.5	0.5	1.2	0
$|D/J_{ave}|$	0.3	0.3	0.07	0.3
A (meV)	−3.4	−3.9	−0.1	−6.6

VI. DETERMINATION OF THE SPIN ORIENTATIONS OF FE PAIR

The Hamiltonian, Eq. (1), consists of the Heisenberg-Ising term, the DM interaction term, and the SIA term. Here we discuss how these terms influence the orientations of the two Fe spins by using the parameters obtained for the calculations of the $R \approx 4.0$ Å case to show the SIA term is crucial for determining the spin orientation.

First, we consider only the Heisenberg-Ising exchange interactions. The positive J_{ii} (i = x, y, z) makes the two spins have a collinear arrangement in the AFM state. If there is no anisotropy in the exchange interaction, the direction of these two spins is arbitrary. However, in our case, the anisotropy of J_{xx}, J_{yy}, and J_{zz} would lead to a weak preference for the spins to point along the x axis ($J_{xx} > J_{yy}$, J_{zz}).

Second, neglecting the spin exchange and the SIA, we consider only the DM interaction. The term $\mathbf{D} \cdot (\mathbf{S}_1 \times \mathbf{S}_2)$ forces the two spins to be perpendicular to each other to have the maximum energy gain, which gives rise to a competition with the spin exchange that prefers collinear spin arrangements. The large D_y term makes the two spins perpendicular to each other in the xz plane, and the small D_z term makes the spins slightly out of the xz plane.

Now we take the spin exchange and the DM interactions together. As a result of competition between the two interactions, we have AFM state along the x axis dictated by J_{xx} ($> J_{yy}$, J_{zz}). Because the moment cancels along the x axis, there must be canted moments along the z and the y axes due to the DM interactions associated with D_y and D_z, respectively [see Fig. 7(a)].

Finally, we take the effect of the SIA into account. Obviously, the large A forces the two spins to be (anti)parallel to the z axis, overcoming their weak preference to align along the x direction. Now, we have the AFM state with spins along the z axis, which utilizes the J_{zz} component and has no conflict with A. In this case, the large D_y forces the two spins to be aligned along the x axis, thus leaving a canted moment along this direction. The J_{yy} term puts the two spins antiparallel along the y axis, and this is also favored by the small D_z because a canted moment already exists along the x axis [see Fig. 7(b)].
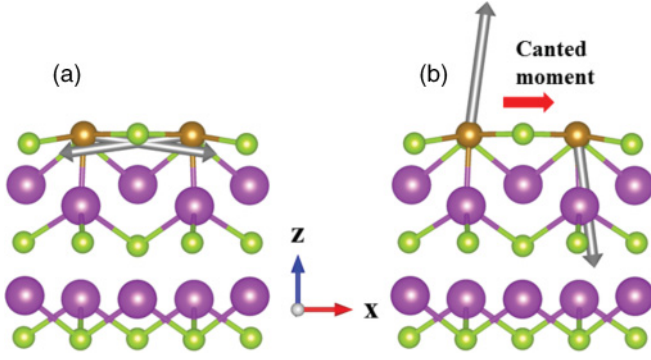
FIG. 7. (Color online) The spin orientations predicted (a) in the absence and (b) in the presence of SIA by using the model Hamiltonian with the parameters determined from first-principles DFT calculations. (b) When considering SIA, a canted moment is left (red arrow) along the x axis, and this canted moment could be delicately controlled by an external electric field.

Taken together, the SIA makes the spins of the magnetic adatoms to align along the z axis. Without the SIA, the spins lie nearly in the xz plane because of the large J_{xx} and D_y. In the model Hamiltonian study of Zhu *et al.*,[11] in which the SIA and D_z terms are not included, and $J_{zz} = J_{xx} \neq J_{yy}$, there would be no anisotropy in the xz plane. However, our calculations predict an anisotropic magnetic behavior along all the x, y, and z directions. This difference can be tested experimentally.

VII. EFFECT OF ELECTRIC FIELD

Results of our calculations with external electric field applied along the c direction are summarized in Fig. 8(a) for the case of the R ≈ 4.0 Å Fe dimer, and in our calculations the positive field direction is along the positive direction of the c axis. The difference charge density plot obtained from the densities calculated for the electric fields of -1.2 V/Å and 0 [Fig. 8(b)] shows that with negative electric field, electrons are transferred from the lower surface to the upper one. In their model Hamiltonian analysis of the RKKY interaction between magnetic atoms on the surface of a TI, Zhu *et al.*[11] concluded that the Fermi level can be tuned by electric field, and the magnetization can be controlled as a consequence. Indeed, our calculations with electric field applied along the c axis show that the magnetic interactions are delicately controlled by electric field. Increasing the electric field weakens the Heisenberg-Ising spin exchanges but strengthens the DM interaction, raising the $|D/J_{ave}|$ ratio up to ~0.6, in support of the finding by Zhu *et al.*[11] Our 1QL-slab is too thin to apply a large electric field. However, with thicker slabs consisting of multiple QLs, a much stronger electric field can be applied to achieve $J_{ii} \approx 0$ so that a pure DM system can be realized, as suggested by Zhu *et al.*[11]

With the parameters of the model Hamiltonian [Eq. (1)] determined by density functional calculations [Fig. 8(a)], one can derive the most stable spin configuration at a given electric field. Our results for the case of R ≈ 4 Å show that the total magnetic moment of the Fe pair cancels along the y and z axes (i.e., in AFM arrangement), but a tunable canted moment remains along the x axis due to the large D_y [see Sec. VI and Fig. 7(b)], and this canted moment could be delicately
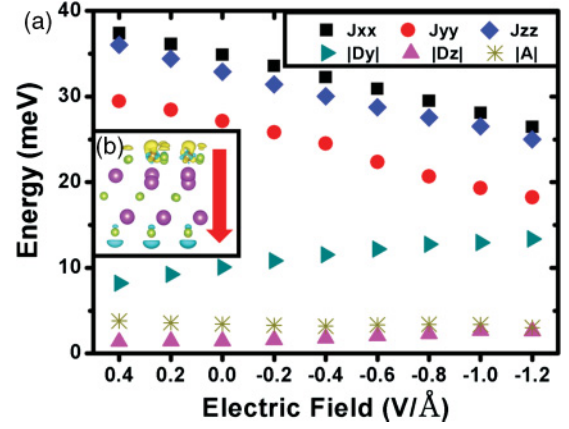

FIG. 8. (Color online) The effect of an electric field E along the c direction on the magnetic interaction parameters and the difference charge density distribution of the (111) surface of Bi_2Se_3 with Fe atoms adsorbed at the nearest-neighbor B sites: (a) The dependence of the spin exchange, the DM vector, and the SIA term on E. (b) The difference charge density distribution, $\Delta\rho = \rho(E) - \rho(0)$, where $\rho(E)$ is the charge distribution under $E = -1.2 V/Å$ and $\rho(0)$ is that without applied electric field. The negative field points down in this figure as shown with the red/dark gray arrow. The blue/medium gray area denotes charge loss, and the yellow/light gray area denotes charge accumulation.

controlled by the electric field. By analogy to the surface magnetoelectric effect observed for thin films,[21] we describe how the surface magnetic moment depends on applied electric field by calculating the surface magnetoelectric coefficient α_s[21]

$$\alpha_s = \mu_0 \Delta M / E, \qquad (2)$$

where ΔM is the magnetization introduced by the applied electric field E and μ_0 is the magnetic permeability of free space. By linearly fitting the calculated magnetic moment as a function of E, we obtain $\alpha_s \approx -2.8 \times 10^{-13} Gcm^2/V$, which is much larger than the surface magnetoelectric coefficient of Fe film ($\alpha_s \approx 2.9 \times 10^{-14} Gcm^2/V$).[21] This suggests that the total magnetization of a TI possessing magnetic adatoms on its surface can be delicately controlled by electric field.

VIII. SIMULATION WITH 2QL- AND 4QL-SLABS

To validate the use of the results resulting from the 1QL-slab model of Bi_2Se_3, we calculate the J_{zz}, J_{yy}, D_y and A values for two Fe adatoms (with R ≈ 4.0 Å) adsorbed on 2QL- and 4QL-slabs. It is noted that a pristine 4QL-slab exhibits a surface Dirac cone,[6] and a pristine 3QL-slab, which opens a small band gap at the Dirac cone, was used to study the TSS by

TABLE III. Some parameters calculated with 1QL-, 2QL-, and 4QL-slabs to validate the results from the calculations using 1QL-slab.

	J_{yy} (meV)	J_{zz} (meV)	D_y (meV)	A (meV)
1QL-slab	27.1	32.9	-10.1	-3.4
2QL-slab	32.3	36.8	-7.1	-3.8
4QL-slab	30.5	33.8	-8.3	-5.1

density functional calculations.[4] We construct the structures of 2QL- and 4QL-slabs by using the 1QL-slab described as the topmost QL holding the Fe adatoms and then by adding other QL(s) taken from the pristine Bi_2Se_3 bulk below the topmost QL. The results of our calculations performed with a $4 \times 4 \times 1$ supercell by using a $3 \times 3 \times 1$ k point set are listed in Table III. Although the calculated values fluctuate slightly with the increasing QL numbers, the strong anisotropy in exchange interactions, the large $|D/J|$ (i.e., $|D/J_{ave}|$) ratio and the large negative A remain unchanged, and the relationship between J_{zz}, J_{yy}, and D_y in the 2QL- and 4QL-slabs is very similar to that observed for the 1QL-slab. These results ensure that our results from the calculations on the 1QL-slab are valid.

IX. CONCLUSIONS

The essential elements needed in describing the magnetic interactions between Fe adatoms on the surface of the TI Bi_2Se_3 are the anisotropic Heisenberg-Ising spin exchange, the DM interaction, and the SIA. All these effects originate substantially from the interactions of the magnetic adatoms with the TSS conducting electrons. The DM interaction is strong with $|D/J| \approx 0.3$, and the ratio can be further increased to ~ 0.6 by an electric field applied along the z axis. The apparent SIA of magnetic adatoms should not be neglected.

APPENDIX A: THE DEMONSTRATION OF //c PREFERENCE OF Bi* SPIN UNDER SOC EFFECT

The three states $|p_z, \uparrow\rangle$, $|p_x, \downarrow\rangle$, and $|p_y, \downarrow\rangle$ of Bi* become split under the action of SOC. We use SOC Hamiltonian $H_{SO} = \lambda L \cdot S$, where λ is the SOC constant ($\lambda > 0$ for the case of one electron occupying the three p-states), and the $L \cdot S$ term is written as[20]

$$
\begin{aligned}
L \cdot S = S_n \Bigg(& L_z\cos\theta + \frac{1}{2}L_+e^{-i\phi}\sin\theta + \frac{1}{2}L_-e^{i\phi}\sin\theta \Bigg) \\
& + \frac{1}{2}S_+\Bigg(-L_z\sin\theta - L_+e^{-i\phi}\sin^2\frac{\theta}{2} + L_-e^{i\phi}\cos^2\frac{\theta}{2} \Bigg) \\
& + \frac{1}{2}S_-\Bigg(-L_z\sin\theta + L_+e^{-i\phi}\cos^2\frac{\theta}{2} - L_-e^{i\phi}\sin^2\frac{\theta}{2} \Bigg),
\end{aligned}
\tag{A1}
$$

where θ and ϕ are the zenith and azimuth angles of the spin direction **n**. In terms of the spherical harmonics, the three p-states are expressed as

$$
\begin{aligned}
|p_z, \uparrow\rangle &= \left| Y_1^0, \uparrow \right\rangle \\
|p_x, \downarrow\rangle &= \left| \frac{1}{\sqrt{2}}(Y_1^1 + Y_1^{-1}), \downarrow \right\rangle \\
|p_y, \downarrow\rangle &= \left| \frac{-i}{\sqrt{2}}(Y_1^1 - Y_1^{-1}), \downarrow \right\rangle.
\end{aligned}
\tag{A2}
$$

By applying HSO on the three p-states, we can obtain the matrix M,

$$
M = \begin{pmatrix} |p_z, \uparrow\rangle \\ |p_x, \downarrow\rangle \\ |p_y, \downarrow\rangle \end{pmatrix} H_{SO}(|p_z, \uparrow\rangle |p_x, \downarrow\rangle |p_y, \downarrow\rangle).
\tag{A3}
$$

Because of the rotational symmetry of Bi*, we take $\phi = 0$ in Eq. (A1). We consider two spin orientations, $\theta = 0$ and $\frac{\pi}{2}$, for which the spin of Bi* is parallel and perpendicular to the z axis, respectively. (a) For $\theta = 0$, we have

$$
M = \frac{\lambda\hbar^2}{2} \begin{pmatrix} 0 & 1 & -i \\ 1 & 0 & i \\ i & -i & 0 \end{pmatrix}.
\tag{A4}
$$

The eigenvalues and the corresponding eigenvectors are given as follow and in Fig. 4,

$$
\begin{aligned}
E_1 &= -\lambda\hbar^2, & \psi_1 &= \frac{1}{\sqrt{3}}(i|p_z, \uparrow\rangle - i|p_x, \downarrow\rangle + |p_y, \downarrow\rangle), \\
E_2 &= \frac{\lambda\hbar^2}{2}, & \psi_2 &= \frac{1}{\sqrt{2}}(|p_z, \uparrow\rangle + |p_x, \downarrow\rangle), \\
E_3 &= \frac{\lambda\hbar^2}{2}, & \psi_3 &= \frac{1}{\sqrt{2}}(|p_z, \uparrow\rangle + i|p_y, \downarrow\rangle).
\end{aligned}
\tag{A5}
$$

(b) For $\theta = \frac{\pi}{2}$, we have

$$
M' = \frac{\lambda\hbar^2}{2} \begin{pmatrix} 0 & 0 & -i \\ 0 & 0 & 0 \\ i & 0 & 0 \end{pmatrix},
\tag{A6}
$$

and

$$
\begin{aligned}
E'_1 &= 0, & \psi'_1 &= |p_x, \downarrow\rangle, \\
E'_2 &= -\frac{\lambda\hbar^2}{2}, & \psi'_2 &= \frac{1}{\sqrt{2}}(|p_z, \uparrow\rangle - i|p_y, \downarrow\rangle), \\
E'_3 &= \frac{\lambda\hbar^2}{2}, & \psi'_3 &= \frac{1}{\sqrt{2}}(|p_z, \uparrow\rangle + i|p_y, \downarrow\rangle).
\end{aligned}
\tag{A7}
$$

These results are also drawn in Fig. 4.

APPENDIX B: DETERMINATION OF THE PARAMETERS FOR THE SPIN HAMILTONIAN FROM FIRST-PRINCIPLES DENSITY FUNCTIONAL CALCULATIONS BY ENERGY-MAPPING ANALYSIS

The spin Hamiltonian describing the interaction between Fe adatoms on the surface of a TI can be written as [i.e., Eq. (1)]

$$
\begin{aligned}
H = &\left(J_{zz}S_1^z S_2^z + J_{xx}S_1^x S_2^x + J_{yy}S_1^y S_2^y \right) + \mathbf{D} \cdot (\mathbf{S}_1 \times \mathbf{S}_2) \\
&+ A\left[(S_1^z)^2 + (S_2^z)^2 \right].
\end{aligned}
\tag{B1}
$$

To carry out energy-mapping analysis, we select different broken-symmetry spin configurations and determine the energy of each state from first-principles calculations. We use the notation $E(S_1^{(S^x,S^y,S^z)}, S_2^{(S^x,S^y,S^z)})$ to represent the energy of the specific spin configuration, where $S_i^{(S^x,S^y,S^z)}$ ($i = 1, 2$) is the spin orientation of each spin. Here we treat each spin as unit vectors, i.e., $|\mathbf{S_i}| = 1$ ($i = 1, 2$).

The Heisenberg-Ising terms are obtained as follows:

$$2J_{xx} = E\big(S_1^{(1,0,0)},S_2^{(1,0,0)}\big) - E\big(S_1^{(1,0,0)},S_2^{(-1,0,0)}\big),$$

$$2J_{yy} = E\big(S_1^{(0,1,0)},S_2^{(0,1,0)}\big) - E\big(S_1^{(0,1,0)},S_2^{(0,-1,0)}\big), \quad \text{(B2)}$$

$$2J_{zz} = E\big(S_1^{(0,0,1)},S_2^{(0,0,1)}\big) - E\big(S_1^{(0,0,1)},S_2^{(0,0,-1)}\big).$$

The direction of the DM vector **D** is constrained by the spatial structural symmetry,[20] and we first carry out the symmetry analysis and then perform the DFT calculations and check if they are consistent. In all cases, $\mathbf{R} = \mathbf{r}_2 - \mathbf{r}_1$ is set to be the positive direction of the x axis. Considering the case of R $\approx$ 4.0 Å, this structure has a mirror plane perpendicular to **R**, locating at the midpoint of the segment linking the two adatoms. In this case, **D** is parallel to the mirror plane, i.e., $D_x = 0$.[20] From the density functional point of view, we have

$$2D_x = E\big(S_1^{(0,1,0)},S_2^{(0,0,1)}\big) - E\big(S_1^{(0,0,-1)},S_2^{(0,-1,0)}\big),$$

$$2D_y = E\big(S_1^{(0,0,-1)},S_2^{(-1,0,0)}\big) - E\big(S_1^{(1,0,0)},S_2^{(0,0,1)}\big), \quad \text{(B3)}$$

$$2D_z = E\big(S_1^{(1,0,0)},S_2^{(0,1,0)}\big) - E\big(S_1^{(0,-1,0)},S_2^{(-1,0,0)}\big).$$

When R $\approx$ 7.2 Å, the structure has a mirror plane parallel to **R**, containing the two adatoms. This would lead **D** perpendicular to the mirror plane, i.e., $D_x = 0$ and $D_z = 0$.[20] In terms of first-principles DFT calculations, we have

$$2D_x = E\big(S_1^{(0,1,0)},S_2^{(0,0,1)}\big) - E\big(S_1^{(0,1,0)},S_2^{(0,0,-1)}\big),$$

$$2D_y = E\big(S_1^{(1,0,0)},S_2^{(0,0,-1)}\big) - E\big(S_1^{(1,0,0)},S_2^{(0,0,1)}\big), \quad \text{(B4)}$$

$$2D_z = E\big(S_1^{(1,0,0)},S_2^{(0,1,0)}\big) - E\big(S_1^{(1,0,0)},S_2^{(0,-1,0)}\big).$$

The results from our DFT calculations are consistent with the symmetry analyses here.

The SIA energy A is simply given by $A = E_{//c} - E_{\perp c}$ for the case of an isolated adatom. For the case of two adatoms interacting, it is obtained as

$$2A = E\big(S_1^{(0,0,1)},S_2^{(0,0,1)}\big) - E\big(S_1^{(1,0,0)},S_2^{(1,0,0)}\big) - J_{zz} + J_{xx},$$

$$\text{or} \quad 2A = E\big(S_1^{(0,0,1)},S_2^{(0,0,1)}\big) - E\big(S_1^{(0,1,0)},S_2^{(0,1,0)}\big) - J_{zz} + J_{yy}.$$

(B5)

*hxiang@fudan.edu.cn

†xggong@fudan.edu.cn

[1]H. Zhang, C.-X. Liu, X.-L. Qi, X. Dai, Z. Fang, and S.-C. Zhang, Nat. Phys. **5**, 438 (2009).

[2]Yi Zhang, K. He, C.-Z. Chang, C.-L. Song, L.-L. Wang, X. Chen, J.-F. Jia, Z. Fang, X. Dai, W.-Y. Shan, S.-Q. Shen, Q. Niu, X.-L. Qi, S.-C. Zhang, X.-C. Ma, and Q.-K. Xue, Nat. Phys. **6**, 584 (2010).

[3]L. A. Wray, S.-Y. Xu, Y. Xia, D. Hsieh, A. V. Fedorov, Y. S. Hor, R. J. Cava, A. Bansil, H. Lin, and M. Z. Hasan, Nat. Phys. **7**, 32 (2011).

[4]H. Chen, W. Zhu, D. Xiao, and Z. Zhang, Phys. Rev. Lett. **107**, 056804 (2011).

[5]M. Z. Hasan and C. L. Kane, Rev. Mod. Phys. **82**, 3045 (2010).

[6]T. M. Schmidt, R. H. Miwa, and A. Fazzio, Phys. Rev. B **84**, 245418 (2011).

[7]J. Honolka, A. A. Khajetoorians, V. Sessi, T. O. Wehling, S. Stepanow, J.-L. Mi, B. B. Iversen, T. Schlenk, J. Wiebe, N. Brookes, A. I. Lichtenstein, Ph. Hofmann, K. Kern, and R. Wiesendanger, e-print arXiv:1112.4621 (2011, to be published).

[8]Q. Liu, C.-X. Liu, C. Xu, X.-L. Qi, and S.-C. Zhang, Phys. Rev. Lett. **102**, 156603 (2009).

[9]R. R. Biswas and A. V. Balatsky, Phys. Rev. B **81**, 233405 (2010).

[10]C. W. Niu, Y. Dai, M. Guo, W. Wei, Y. Ma, and B. Huang, App. Phys. Lett. **98**, 252502 (2011).

[11]J.-J. Zhu, D.-X. Yao, S.-C. Zhang, and K. Chang, Phys. Rev. Lett. **106**, 097201 (2011).

[12]R. Yu, W. Zhang, H.-J. Zhang, S.-C. Zhang, X. Dai, and Z. Fang, Science **329**, 61 (2010).

[13]H. J. Xiang, E. J. Kan, M.-H. Whangbo, C. Lee, S.-H. Wei, and X. G. Gong, Phys. Rev. B **83**, 174402 (2011); H. J. Xiang, E. J. Kan, S.-H. Wei, M.-H. Whangbo, and X. G. Gong, *ibid.* **84**, 224429 (2011); H. J. Xiang, E. J. Kan, Y. Zhang, M.-H. Whangbo, and X. G. Gong, Phys. Rev. Lett. **107**, 157202 (2011).

[14]G. Kresse and J. Furthmüller, Phys. Rev. B **54**, 11169 (1996).

[15]P. E. Blöchl, Phys. Rev. B **50**, 17953 (1994).

[16]G. Kresse and D. Joubert, Phys. Rev. B **59**, 1758 (1999).

[17]J. P. Perdew, K. Burke, and M. Ernzerhof, Phys. Rev. Lett. **77**, 3865 (1996).

[18]Y. Sakamoto, T. Hirahara, H. Miyazaki, S.-i. Kimura, and S. Hasegawa, Phys. Rev. B **81**, 165432 (2010).

[19]J. Neugebauer and M. Scheffler, Phys. Rev. B **46**, 16067 (1992).

[20]D. Dai, H. J. Xiang, and M.-H. Whangbo, J. Comput. Chem. **29**, 13 (2008).

[21]C.-G. Duan, J. P. Velev, R. F. Sabirianov, Z. Zhu, J. Chu, S. S. Jaswal, and E. Y. Tsymbal, Phys. Rev. Lett **101**, 137201 (2008).